

See discussions, stats, and author profiles for this publication at: <https://www.researchgate.net/publication/261329555>

# 8% Efficient $\text{Cu}_2\text{ZnSn}(\text{S},\text{Se})_4$ solar cells from redox equilibrated simple precursors in DMSO

ARTICLE in ADVANCED ENERGY MATERIALS · AUGUST 2014

Impact Factor: 16.15 · DOI: 10.1002/aenm.201301823

---

CITATIONS

21

---

READS

154

4 AUTHORS, INCLUDING:



Hao Xin

University of Washington Seattle

22 PUBLICATIONS 1,114 CITATIONS

SEE PROFILE



John Katahara

University of Washington Seattle

5 PUBLICATIONS 27 CITATIONS

SEE PROFILE

# 8% Efficient $\text{Cu}_2\text{ZnSn}(\text{S},\text{Se})_4$ Solar Cells from Redox Equilibrated Simple Precursors in DMSO

Hao Xin, John K. Katahara, Ian L. Braly, and Hugh W. Hillhouse\*

Kesterite-based thin film photovoltaic cells using copper zinc tin sulfide, selenide, and sulfoselenide,  $\text{Cu}_2\text{ZnSnS}_4$  (CZTS),  $\text{Cu}_2\text{ZnSnSe}_4$  (CZTSe), and  $\text{Cu}_2\text{ZnSn}(\text{S},\text{Se})_4$  (CZTSSe), respectively, as absorber layer are very promising for inexpensive photovoltaic electricity generation due to the Earth abundance and low-toxicity of the materials, and the rapid improvement in power conversion efficiency from this family of compounds.<sup>[1]</sup> Many approaches have been developed to fabricate kesterite thin films, such as vacuum based deposition,<sup>[2,3]</sup> chemical vapor deposition,<sup>[4]</sup> electrodeposition,<sup>[5]</sup> and solution-based processing.<sup>[6–11]</sup> Solution-based processing approaches can be further sub-divided based on whether the kesterite is formed before applying the liquid coating (as with many nanocrystal-ink approaches)<sup>[6]</sup> or is formed only after reactions that occur in the precursor layer after liquid coating (as in hydrazine slurry based approaches<sup>[1,9,12]</sup> and molecular-ink approaches).<sup>[7,11,13]</sup> Among these techniques, forming films directly from molecular-inks that are true solutions (not slurries) and formulated without toxic solvents or ligands like hydrazine are the most promising for low-cost sustainably-produced CZTS solar cells due to the simplicity, high material utilization, facile control of the precursor ratios, low-toxicity, and reduced environmental or safety concerns (especially when compared to hydrazine based inks).

Our group has previously reported that CZTSSe films can be processed from a molecular-ink using an environmentally benign solvent dimethyl sulfoxide (DMSO), yielding solar cells with a power conversion efficiency of 4.1%.<sup>[7]</sup> The solution was made by simultaneously dissolving copper, zinc, and tin containing compounds, and thiourea in DMSO (Figure 1a). The CZTSSe film was fabricated by spin-coating and annealing the precursor solution to form a CZTS film first, followed by annealing the film at 500 °C with elemental selenium vapor (so called selenization) to partially replace sulfur and increase film crystallinity. Here, using the same precursor materials and target film composition, we developed a different solution preparation process that explicitly relies on redox equilibration of the precursors. The resulting inks yield better quality CZTS. Furthermore, we have decreased film thickness and increased

selenization temperature to obtain a 900 nm CZTSSe film with larger grain size. Upon full device processing on this film, a solar cell with an active area power conversion efficiency of 8.3% was achieved without an antireflection coating on a cell with an area of 0.43 cm<sup>2</sup>. These early experiments show the importance of redox reaction in solution as well as the optimization of device fabrication conditions.

The improved precursor solutions were made by adding the precursors into the solvent step-by-step as shown in Figure 1b. First, 4 mL DMSO was added to a vial containing 4 mM

$\text{Cu}(\text{OAc})_2 \cdot \text{H}_2\text{O}$ , resulting in a deep blue suspension due to very limited solubility of  $\text{Cu}(\text{OAc})_2 \cdot \text{H}_2\text{O}$  in DMSO. Second, precursor  $\text{SnCl}_2 \cdot 2\text{H}_2\text{O}$  (2.75 mM) was added into the vial, and the deep blue suspension gradually changed to clear light green solution after overnight stirring. Adding the third precursor  $\text{ZnCl}_2$  (2.80 mM) into the solution resulted in further color change from light green to lighter green, with a yellow tint. Finally, 13.2 mM thiourea was added, and a transparent and colorless solution was obtained after thiourea completely dissolved. The change from deep blue suspension to a very light green-yellow clear solution after the first two steps indicates reduction of  $\text{Cu}^{2+}$  to  $\text{Cu}^+$  (Equation (1)) accompanied by solvation/stabilization of metal ions by DMSO and/or chloride anions. The final colorless solution indicates that little  $\text{Cu}^{2+}$  remains after adding thiourea. The data suggest that complexation between metal ions and thiourea form more stable  $\text{Cu}^+$  species which assist the reduction of the remaining  $\text{Cu}^{2+}$  to  $\text{Cu}^+$ .



In contrast to the previous approach, in which all precursors are added simultaneously and the redox and complexation reactions compete and may result in kinetically stabilized solutions with remaining  $\text{Cu}^{2+}$ , the current procedure provides a pathway for the redox reaction to complete which greatly reduces the amount of  $\text{Cu}^{2+}$ . The yellow color in the previous solution (Figure 1a) is due to unreacted  $\text{Cu}^{2+}$  which form  $\text{CuCl}_4^{2-}$  (a yellow species) in high  $\text{Cl}^-$  containing solution (note that solvated  $\text{Zn}^{2+}$ ,  $\text{Sn}^{2+}$ , and  $\text{Sn}^{4+}$  result in colorless solutions). The detailed chemistry in the precursor solution is still under investigation, and the results will be reported in follow-up work.

The redox-equilibrated precursor solution (meaning that the redox-reaction has equilibrated) as reported here is very stable; no precipitation or color change has been observed after several months stored in sealed vial at room temperature. The solution was diluted by 35% with DMSO before it was spin-coated on a molybdenum coated soda-lime-glass (SLG) substrate to form the precursor film. Seven coatings were applied for a total

Dr. H. Xin, J. K. Katahara, I. L. Braly,  
Prof. H. W. Hillhouse  
Department of Chemical Engineering  
and the Molecular Engineering and Sciences Institute  
University of Washington, Box 351750,  
Seattle, WA 98195–1750, USA  
E-mail: h2@uw.edu



DOI: 10.1002/aenm.201301823

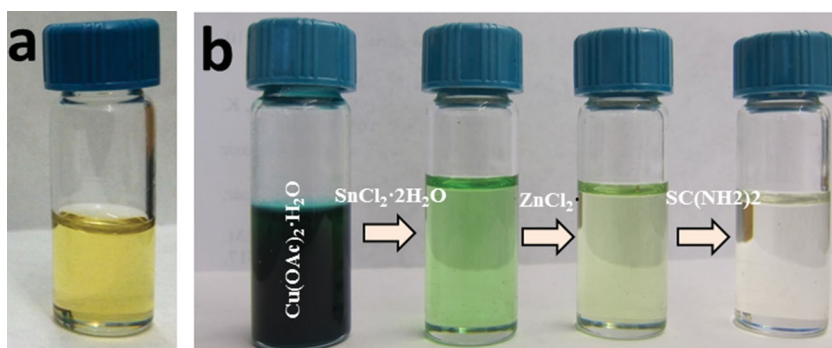


**Figure 1.** Photograph of a) solution made by dissolving all precursors simultaneously in solvent and b) solutions in each step of the precursor solution preparation. Note the difference in solution color.

thickness of approximately 900 nm after selenization. After each coating, the films were annealed on a 540 °C hotplate for 2.5 min. The films were then annealed with elemental Se in a vented graphite box at temperature of 540 °C (instead of 500 °C)<sup>[7]</sup> for 20 min to form CZTSSe.<sup>[14]</sup> The devices were finished in a standard procedure as described in a previous report including: a 40 nm CdS buffer layer by chemical bath deposition, a 50 nm i-ZnO and 250 nm ITO window layer by RF sputtering, and top contact of Ni/Al by thermal deposition.<sup>[7]</sup> The detailed experiments are given in the SI.

**Figure 2a** shows the current density–voltage ( $J$ – $V$ ) characteristics of the best performing solar cell measured under dark and simulated AM1.5 illumination. A power conversion efficiency (PCE) of 8.32% was achieved based on an active area of 0.43 cm<sup>2</sup> with a short circuit current density ( $J_{sc}$ ) of 31.2 mA cm<sup>−2</sup>, an open circuit voltage ( $V_{oc}$ ) of 0.443 V, and a fill factor ( $FF$ ) of 0.602. The series resistance ( $R_s$ ), shunt resistance ( $R_{sh}$ ), diode ideality factor ( $n$ ), and reverse saturation current prefactor ( $J_0$ ) extracted from the  $J$ – $V$  curves by non-linear least squares fit of the non-ideal diode equation (expressed with the Lambert-W function) are 0.88 Ω cm<sup>2</sup>, 229 Ω cm<sup>2</sup>, 2.02, and  $6.0 \times 10^{-3}$  mA cm<sup>−2</sup>, respectively. All the device parameters are listed in the inset of Figure 2a. Compared to the previous device,<sup>[7]</sup> improvements are achieved in all three device parameters with  $J_{sc}$ ,  $V_{oc}$ ,

and  $FF$  enhanced by 22%, 10%, and 46%, respectively, which accounts for the doubled overall efficiency. The dark and light  $J$ – $V$  curves of the current device are close to superposition (cross over point at 74 mA cm<sup>−2</sup>). The normally observed cross over behavior in hydrazine based devices,<sup>[1,10,15]</sup> which has been associated with a back-contact barrier by some,<sup>[15,16]</sup> is not present in the current device. Among the 6 devices on the same substrate (Figure 2a, inset), efficiencies in the range of 6.18–8.32% with an average of 7.15% and standard deviation of 0.91 were achieved, indicating good film uniformity. We note that due to the suboptimal geometry of the top contact mask, the electrode grid (0.10 cm<sup>2</sup>)

shades 19% of the device area (Figure 2a, inset), which lowers the total area efficiency to 6.75%. Using a more optimal mask, which generally results in a 4% grid shadow,<sup>[17]</sup> the total area efficiency should be 8.0%. Compared to the record CZTSSe solar cell,<sup>[1]</sup> the overall efficiency in the current device is limited by low  $FF$  mainly due to low shunt resistance (229 Ω cm<sup>2</sup>), high series resistance (0.88 Ω cm<sup>2</sup>), and high diode quality factor (2.02). The addition of a standard MgF<sub>2</sub> antireflective coating should increase the total area efficiency to around 9%.

The external quantum efficiency (EQE) of the champion molecular precursor device is shown in Figure 2b. The EQE exceeds 80% in the visible range but gradually decays for longer wavelength. The loss at longer wavelength is likely caused by short carrier diffusion length (low mobility-lifetime product) and/or insufficient penetration of the depletion range into the absorber. To identify the carrier collection loss mechanism, reverse biased EQE at −1 V was measured, and the quantum efficiency ratio of EQE(−1 V)/EQE(0 V) was plotted on the top panel of Figure 2b. As expected, the bias ratio slightly increases at longer wavelength, confirming the minority carrier losses in the quasi-neutral region. In addition, the EQE(−1 V)/EQE(0 V) ratio is well above 1.05 over the entire wavelength range regardless of where the carriers are generated, suggesting significant recombination at the interface or near the junction.<sup>[17]</sup>

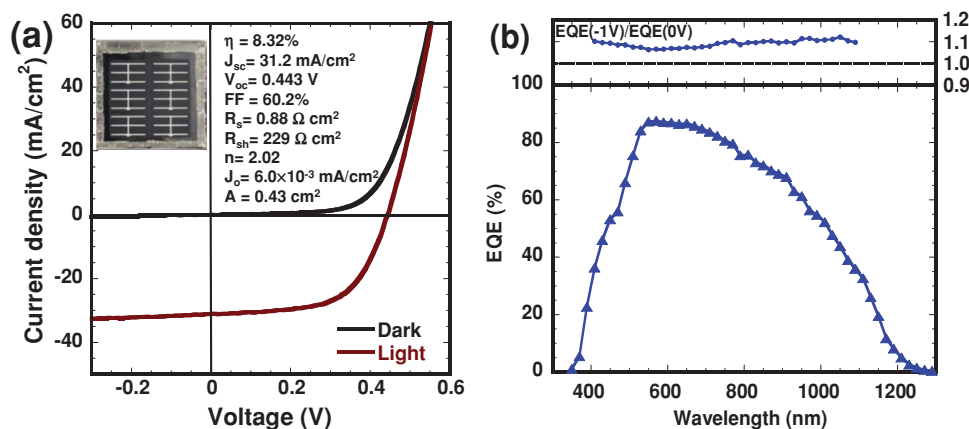


**Figure 2.** a)  $J$ – $V$  characteristics of the best performing CZTSSe solar cell measured in dark and under AM 1.5 simulated sunlight. The device parameters are calculated based on active area of 0.43 cm<sup>2</sup>. Inset: photograph of the six CZTSSe devices on one substrate. b) External quantum efficiency (EQE) of the highest efficiency CZTSSe solar cell. Top panel: EQE ratio at −1 and 0 V biased voltage.

Although a wavelength-independent biased EQE ratio above one was not observed in other high performance CZTSSe solar cells,<sup>[1,10,12,15,18]</sup> interface recombination was also identified by temperature dependent  $V_{oc}$  study.<sup>[15]</sup>

To further identify if a short depletion range is a problem in the current device, room temperature drive-level capacitance profiling (DLCP) and capacitance voltage (C-V) measurements were performed.<sup>[19]</sup> The carrier concentrations estimated by DLCP and C-V measurements are  $6.7 \times 10^{15} \text{ cm}^{-3}$  and  $9.7 \times 10^{15} \text{ cm}^{-3}$ , respectively (Supporting Information, Figure S6). The first moment of charge response indicated by DLCP profiles is about 150 nm at zero bias. However, the depletion width calculated assuming uniform doping in a p-n<sup>+</sup> heterojunction with this carrier concentration in the p-type region is about 250 nm. Comparing these two numbers suggests that a significant population of deep-level charged defects is shifting the first moment of charge response toward the junction (and thus reducing the region of high electric field).

The bandgap of the absorber material extracted from the EQE data is 1.11 eV, shown in Figure 3, which is lower than the previously reported DMSO processed CZTSSe film and is very close to that of the record kesterite device processed from hydrazine. The low bandgap accounts for the observed enhancement in  $J_{sc}$  due to efficient light harvesting in near infrared range. Photoluminescence (PL) of the CZTSSe absorber measured on the finished device (Figure 3) shows a single broad asymmetric peak, which is characteristic of highly compensated semiconductors.<sup>[20]</sup> The peak is red shifted by 70 meV from the bandgap due to either tail states or the presence of potential fluctuations, which have been shown to degrade device performance.<sup>[21]</sup> The maximum theoretical quasi Fermi energy level splitting  $\Delta\mu$  was calculated from the spectral flux,  $I_{PL}(E)$ , as described by the generalized Planck law for non-equilibrium emission from a material,<sup>[22]</sup> shown as Equation (2). Here  $h$  is the Planck constant,  $c$  is the speed of light in vacuum,  $a(E)$  is the spectral absorptivity,

$k$  is the Boltzmann constant,  $T$  is the absolute temperature, and  $E$  is the energy of emission.

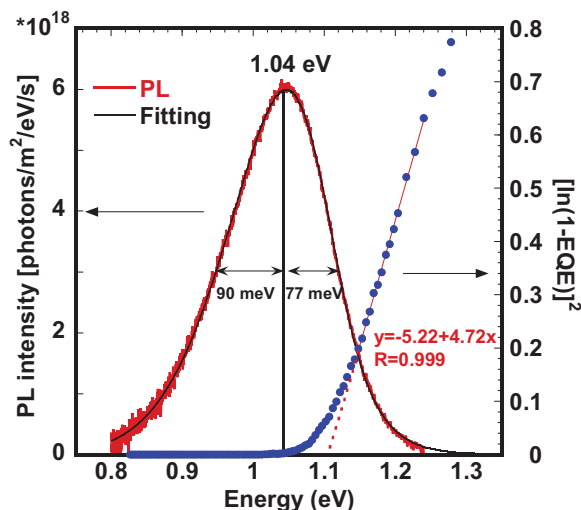
$$I_{PL}(E) = \frac{2\pi}{h^3 c^2} \frac{a(E)E^2}{\exp[(E - \Delta\mu)/kT] - 1} \quad (2)$$

A nonlinear least squares fitting procedure using a Levenberg-Marquardt algorithm is used to extract  $\Delta\mu$  and the decay of the spectral absorptivity. The calculated  $\Delta\mu$  value is 0.46 eV (Figure 3), which is very close to the  $V_{oc}$  measured under simulated AM1.5 illumination.<sup>[23]</sup> The slight difference is due to the fact that these data are collected in a confocal setup (see Supporting Information) and at higher injection than one sun ( $\approx 18$  sun equivalents excitation).

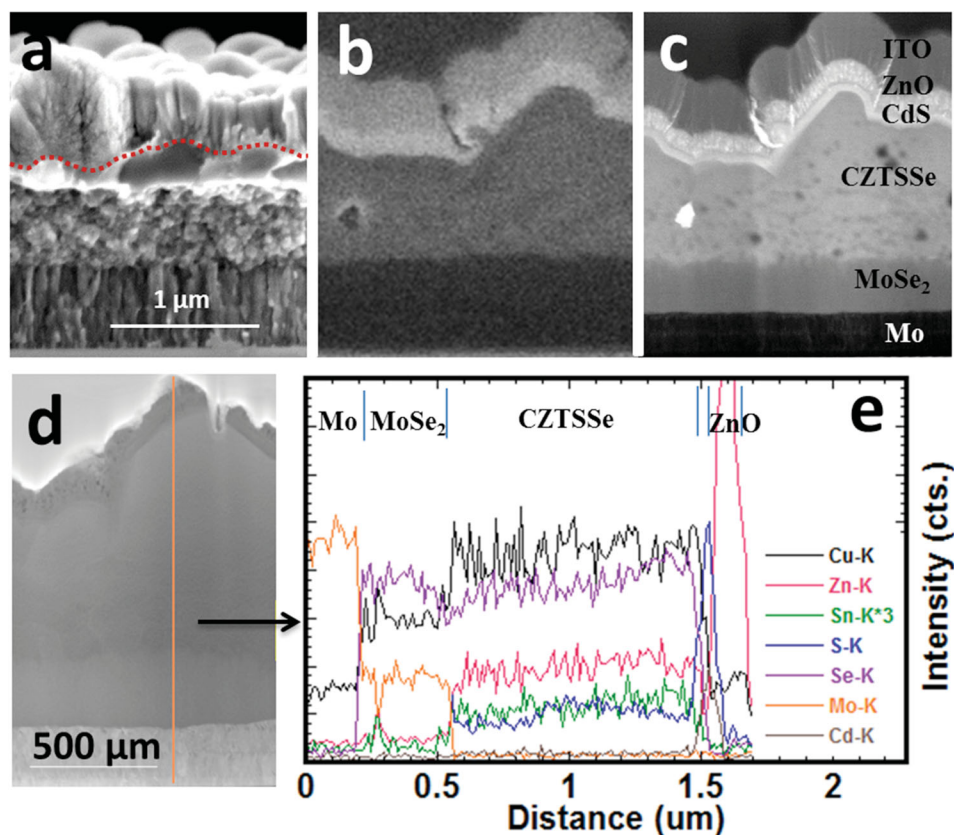
Powder X-ray diffraction (XRD, Supporting Information Figure S1) and Raman spectroscopy (Supporting Information Figure S2) confirmed single kesterite structure (JCPDS 00-052-0868) with no detectable secondary/ternary phases. Top view scanning electron microscopy (SEM) image of the CZTSSe films demonstrated densely packed large grains on the order of microns (Supporting Information Figure S3), and the composition of the absorber determined by energy dispersive X-ray (EDX) analysis is  $\text{Cu}_{1.71}\text{Zn}_{1.12}\text{Sn}_{1.01}(\text{S}_{0.14}\text{Se}_{0.86})_4$  (Supporting Information). The stoichiometry of this absorber material is  $\text{Cu}/(\text{Zn}+\text{Sn}) = 0.80$ ,  $\text{Zn}/\text{Sn} = 1.11$ , and  $\text{S}/(\text{S}+\text{Se}) = 0.14$ , a copper poor and zinc rich makeup that is similar to other high performance absorbers. The  $\text{S}/(\text{S}+\text{Se})$  ratio agrees very well with that calculated from the XRD data, which is 0.20 (Supporting Information).

Figure 4 shows the cross section SEM and TEM images of the as-cleaved device and focused ion beam (FIB)-prepared thin film lamellar. From Figure 4a, it is clear that the absorber consists of two regions: a large-grain top layer and a small-grain bottom layer. The large grains seen on the top view SEM image (Supporting Information Figure S3) do not extend vertically through the absorber layer. The crystallographic grain size calculated from the XRD data is  $\approx 37$  nm (Supporting Information). The non-uniformity of the bottom layer is also clearly seen in low-voltage STEM (LV-STEM) imaging (Figure 4c). The reason for this double layered structure is not clear. It could be due to difference in the temperature versus time profile at the top and bottom of the film, the rate of penetration of Se into the film (Se penetrates the top layer faster), the rate of Sn loss (faster from the top region), or the segregation of zinc or copper into the back contact during selenization. The small grains are generally deleterious to device performance due to increased opportunity for recombination at grain boundaries and/or decreased carrier mobility. Further optimization of the precursor composition in CZTS molecular ink and selenization conditions (temperature, pressure, time) is crucial to fabricate homogeneous CZTSSe absorbers with large grains that achieve higher solar cell efficiency.

However, scanning kelvin probe microscopy studies on CZTSSe show that the grain boundaries are positively charged, which likely act to reflect minority carriers away from the grain boundary and reduce recombination.<sup>[3]</sup> We believe the morphological inhomogeneity may account for the observed carrier collection loss at longer wavelength. Interestingly, although the two layers appear to have dramatic difference in grain structure



**Figure 3.** Emission and absorption characteristics from the completed device. The absolute intensity calibrated PL spectrum of the device is shown along with a nonlinear least squares fit. The bandgap is determined by fitting the expected linear region (for a direct bandgap semiconductor) of the transformed EQE data.



**Figure 4.** a) Cross section SEM images of the cleaved device. The absorber layer consists of microsize grains formed at the top layer and small grains formed at the bottom layer. b) SEM and c) bright-field low voltage-scanning TEM (LV-STEM) images of cross section lamellae. d) Dark-field transmission electron microscopy (TEM) image of a cross section lamella. e) EDX scan taken along the line in (d). Images (a–c) are aligned to show how each layer is correlated. A 400 nm  $\text{MoSe}_2$  layer is clearly seen in (c).

upon fracturing as seen in SEM, EDX line scan (Figure 4d) demonstrates uniform compositional distribution of the elements across the film. A  $\text{MoSe}_2$  layer with a thickness of about 400 nm is observed (Figure 4c), which is also confirmed by XRD data (Supporting Information Figure S1). We note that a significant amount of Cu is detected in the  $\text{MoSe}_2$  layer, which has recently been attributed to an artifact from the TEM specimen preparation.<sup>[24]</sup> While a thin Mo–Se layer may enhance film adhesion and provide an ohmic contact,<sup>[25]</sup> a thicker layer may increase series resistance and lower device performance.<sup>[16]</sup> The 400 nm  $\text{MoSe}_2$  might be one of the reasons for the high series resistance of the device. We note that compared to TEM and SEM technology, LV-STEM image shows significantly improved contrast between different materials/layers (Figure 4). This powerful technique to detect material quality and possibly impurities in CZTS/CZTSSe films has not been demonstrated in the literature before.

In summary, we have demonstrated 8.32% CZTSSe solar cells from molecular precursor solution in an environmentally benign solvent. The doubled efficiency compared to previous devices comes from the redox-equilibrated new precursor solution and the optimization of selenization temperature which result in better absorber material. The performance of the current device is limited by significant interface recombination, potential fluctuation, and high series resistance largely due to imperfect absorber material and contacts. Optimization of pre-

cursor formulation and device fabrication conditions to address the above-mentioned issues is expected to further improve device performance, making this approach the most promising candidate for low-cost kesterite solar cells.

## Supporting Information

Supporting Information is available from the Wiley Online Library or from the author.

## Acknowledgements

This work was supported primarily by the DOE SunShot Program (No. DE-EE00053210) and Rehnberg Chair funds.

Received: November 27, 2013

Revised: March 7, 2014

Published online:

- [1] T. K. Todorov, J. Tang, S. Bag, O. Gunawan, T. Gokmen, Y. Zhu, D. B. Mitzi, *Adv. Energy Mater.* **2013**, 3, 34.
- [2] a) I. Repins, C. Beall, N. Vora, C. DeHart, D. Kuciauskas, P. Dippo, B. To, J. Mann, W.-C. Hsu, A. Goodrich, R. Noufi, *Sol. Energy Mater. Sol. Cells* **2012**, 101, 154; b) A. V. Moholkar, S. S. Shinde,



- G. L. Agawane, S. H. Jo, K. Y. Rajpure, P. S. Patil, C. H. Bhosale, J. H. Kim, *J. Alloys Compd.* **2012**, 544, 145.
- [3] J. B. Li, V. Chawla, B. M. Clemens, *Adv. Mater.* **2012**, 24, 720.
- [4] T. Washio, T. Shinji, S. Tajima, T. Fukano, T. Motohiro, K. Jimbo, H. Katagiri, *J. Mater. Chem.* **2012**, 22, 4021.
- [5] S. Ahmed, K. B. Reuter, O. Gunawan, L. Guo, L. T. Romankiw, H. Deligianni, *Adv. Energy Mater.* **2012**, 2, 253.
- [6] a) Q. Guo, H. W. Hillhouse, R. Agrawal, *J. Am. Chem. Soc.* **2009**, 131, 11672; b) Q. Guo, G. M. Ford, W. C. Yang, B. C. Walker, E. A. Stach, H. W. Hillhouse, R. Agrawal, *J. Am. Chem. Soc.* **2010**, 132, 17384.
- [7] W. Ki, H. W. Hillhouse, *Adv. Energy Mater.* **2011**, 1, 732.
- [8] M. S. Park, D.-H. Kim, S.-J. Sung, H. J. Jo, J.-K. Kang, *IEEE Inter. Conf. Nanotechnology* 11<sup>th</sup>, Portland Marriot, **2011**, 222.
- [9] D. B. Mitzi, O. Gunawan, T. K. Todorov, K. Wang, S. Guha, *Sol. Energy Mater. Sol. Cells* **2011**, 95, 1421.
- [10] S. Bag, O. Gunawan, T. Gokmen, Y. Zhu, T. K. Todorov, D. B. Mitzi, *Energy Environ. Sci.* **2012**, 5, 7060.
- [11] W. B. Yang, H. S. Duan, B. Bob, H. P. Zhou, B. Lei, C. H. Chung, S. H. Li, W. W. Hou, Y. Yang, *Adv. Mater.* **2012**, 24, 6323.
- [12] D. A. R. Barkhouse, O. Gunawan, T. Gokmen, T. K. Todorov, D. B. Mitzi, *Prog. Photovoltaics* **2012**, 20, 6.
- [13] a) W. B. Yang, H. S. Duan, K. C. Cha, C. J. Hsu, W. C. Hsu, H. P. Zhou, B. Bob, Y. Yang, *J. Am. Chem. Soc.* **2013**, 135, 6915; b) T. Schnabel, M. Löw, E. Ahlswede, *Sol. Energy Mater. Sol. Cells* **2013**, 117, 324; c) K. Tanaka, Y. Fukui, N. Moritake, H. Uchiki, *Sol. Energy Mater. Sol. Cells* **2011**, 95, 838.
- [14] C. N. Bucherl, K. R. Oleson, H. W. Hillhouse, *Curr. Opin. Chem. Eng.* **2013**, 2, 168.
- [15] O. Gunawan, T. K. Todorov, D. B. Mitzi, *Appl. Phys. Lett.* **2010**, 97, 3.
- [16] B. Shin, Y. Zhu, N. A. Bojarczuk, S. J. Chey, S. Guha, *Appl. Phys. Lett.* **2012**, 101, 053903.
- [17] S. S. Hegedus, W. N. Shafarman, *Prog. Photovoltaics* **2004**, 12, 155.
- [18] Q. Guo, G. M. Ford, W.-C. Yang, C. J. Hages, H. W. Hillhouse, R. Agrawal, *Sol. Energy Mater. Sol. Cells* **2012**, 105, 132.
- [19] J. T. Heath, J. D. Cohen, W. N. Shafarman, *J. Appl. Phys.* **2004**, 95, 1000.
- [20] A. P. Levanyuk, V. V. Osipov, *Uspekhi Fizicheskikh Nauk* **1981**, 133, 427.
- [21] a) U. Rau, J. H. Werner, *Appl. Phys. Lett.* **2004**, 84, 3735; b) T. Gokmen, O. Gunawan, T. K. Todorov, D. B. Mitzi, *Appl. Phys. Lett.* **2013**, 103, 103506.
- [22] P. Wurfel, *J. Phys. C-Solid State Phys.* **1982**, 15, 3967.
- [23] T. Unold, D. Berkhahn, B. Dimmler, G. H. Bauer, *Eur. Photovoltaic Sol. Energy Conf.* 16<sup>th</sup>, UK **2000**, 736.
- [24] J. T. Watjen, J. J. Scragg, M. Edoff, S. Rubino, C. Platzer-Bjorkman, *Appl. Phys. Lett.* **2013**, 102, 051902.
- [25] N. Kohara, S. Nishiwaki, Y. Hashimoto, T. Negami, T. Wada, *Energy Mater. Sol. Cells* **2001**, 67, 209.